JOURNAL OF MATERIALS SCIENCE **38** (2003) 2861 – 2874

Hydro-abrasive erosion of refractory ceramics

A. W. MOMBER
Department of Mining, Metallurgy and Earth Sciences, Aachen University (RWTH), Aachen, Germany
E-mail: andreas.momber@t-online.de

R. KOVACEVIC
Department of Mechanical Engineering, Southern Methodist University, Dallas, TX, USA

The paper discusses the material removal process in refractory ceramics eroded by hydro-abrasive jets. In particular, bauxite, sintered magnesia, and magnesia chromite are eroded. The influence of abrasive particle velocity, local exposure time, abrasive mass-flow rate, and abrasive type is investigated. Erosion depth, specific erosion rate, and geometry of the generated cavities are measured and analysed. For particle velocity as well as for local exposure time, threshold conditions are identified. At low erosion intensity, target material properties and abrasive type do not affect the material removal process notably. From optical and SEM-microscopy it is further found that the material removal mode changes with the progression of the erosion process. In the upper region of the eroded kerf, the dominating material removal mode is the simultaneous cutting of matrix and inclusion grains (transgranular). In the lower range, the erosion process is characterised by the removal of the binding matrix followed by washing off the inclusion grains (intergranular). The balance between both modes depends on the energy delivered to the erosion site. These observations are explained by assuming a continuous loss in kinetic energy of the abrasive particles during HAE. Some features of non-linear fracture are noticed and suggestions are made how to use non-linear fracture parameters to evaluate erosion resistance.

1. Introduction

The development of high-quality refractory materials by the ceramic industry brought up latent problems involving the machinability of the bricks being manufactured. To produce bricks of complex shape, advanced pressing methods, such as hot isostatic pressing (HIP), have been introduced. Unfortunately, this has led to high production costs and the produced refractory bricks have become very expensive. The fabrication of bricks that, for example, contains small holes is almost impossible.

The technical utilisation of Hydro-Abrasive Erosion (referred to as HAE in the paper) as a machining method could be a possible solution for manufacturing high quality refractory bricks of special shapes and formats. This useful utilisation of a harmful erosion process is very promising in treating difficult-to-machine materials, including refractory ceramics [1]. Possible machining operations include cutting and milling [2, 3] as well as piercing [4]. Fig. 1 shows small-diameter holes drilled into refractory ceramics by HAE.

Probably the first attempt to use HAE for the machining of ceramic materials was made by Kim *et al.* [5]. These authors conducted piercing and cutting experiments on alumina ceramics and could demonstrate that HAE can effectively be used to machine even high-strength ceramics. Later, Freist *et al.* [6] were the first to report about the utilisation of HAE for the three-dimensional machining of alumina ceramics. However, in order to efficiently apply the HAE-process, a sound understanding of the basic erosion process is required. Despite this need, the number of serious investigations on the HAE of refractory ceramics is limited. Kim *et al.* [5] performed a preliminary investigation on the surface quality of eroded ceramic samples. Hunt *et al.* [7] carried out studies about the HAE of hard materials and found that hardness and 'modulus of fracture' (this term was used in the original paper; the correct term would be 'elastic strain energy density') may be insufficient to describe the resistance of the materials. Identical results have been obtained by Matsui *et al.* [8] on ceramics and pre-cracked materials, such as rocks. Systematic investigations on the hardness influence were performed by Wada and Kumon [9] and Wada [10]. The first authors found a pronounced relationship between the erosion rate and the hardness ratio target/abrasive. For silica-nitride ceramics they identified scratching without any cracking as the predominant mode of material removal. Wada [10] developed wear maps for the HAE of ceramics similar to those known from solid-particle erosion [11]. The basic structure of an erosion map is shown in Fig. 2. The author found that the mode of material removal depended on the

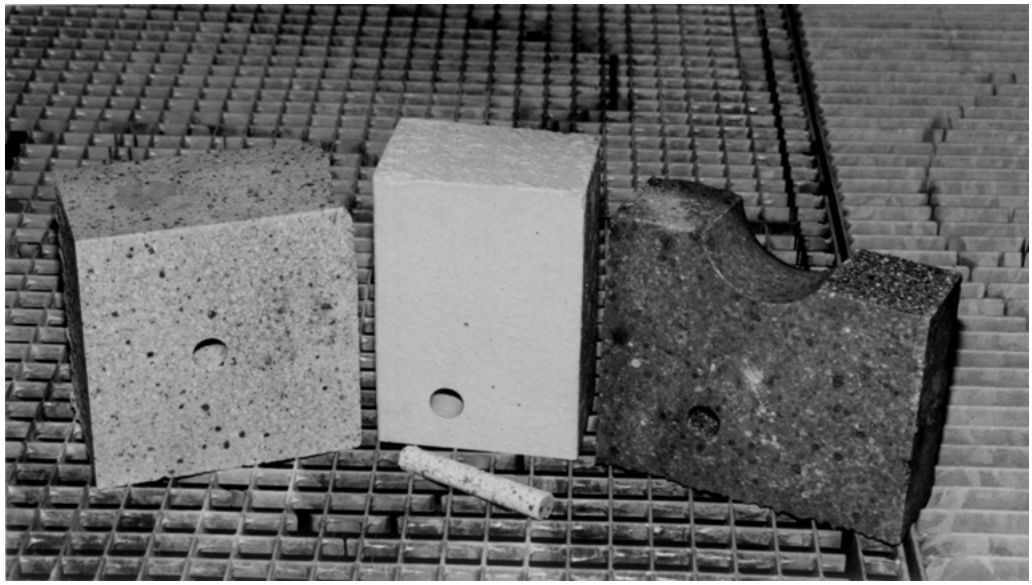

Figure 1 Holes drilled in refractory ceramics by HAE (photo: WOMA Apparatebau GmbH, Duisburg).

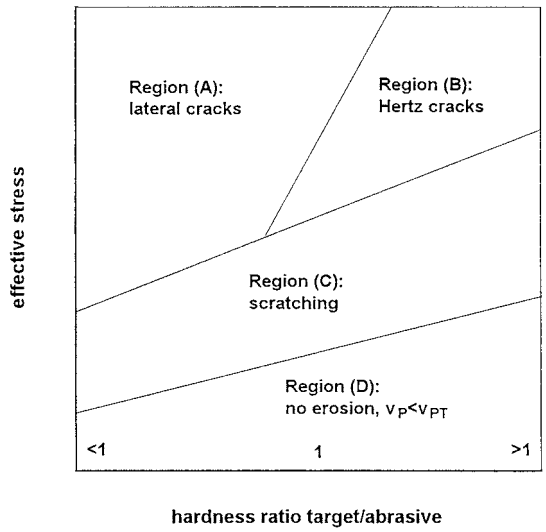

Figure 2 Wear map for the HAE of ceramics [10].

target-abrasive-interaction. SiC-ceramics, for example, were eroded by fracture if SiC- and Al_2O_3-abrasives are used, whereas with garnet-abrasive the material was removed by scratching.

Zeng and Kim [12, 13] investigated the HAE of polycrystalline alumina ceramics. Through SEM-inspections they identified discrete intergranular network cracking and plastic flow at the immediate impact site as dominating material removal modes. The corresponding resistance parameters were found to be the grain size and fracture energy (in the sense of Griffith's surface energy) of the target material. These authors also developed a model for HAE [12]. In a more recent study, Momber *et al.* [14] obtained contrary results. For the HAE of bauxite refractory ceramics, they noted matrix removal, transgranular fracture and interfacial grain pullout. The balance between these modes depended on the energy delivered by the impacting particles. The higher the energy, the higher the probability of transgranular fracture. These observations obtained from SEM-inspections could be verified by acoustic emission measurements. Momber *et al.* [2] also found that the material removal mode was dependent of the erosion depth.

Schwetz *et al.* [15] performed a systematic study about the HAE-resistance of boron-carbide ceramics. Depending on the target material, they noted different material removal modes. Whereas conventional B_4C-ceramics and SiC-ceramics were eroded by lateral transgranular cracking due to surface fatigue, modified B_4C-TiB_2-ceramics failed in two steps: first, the TiB_2-grains were separated from the matrix; second, the boron-carbide matrix cracked transgranularly. Thus, interfacial bond strength played a major role in HAE. This aspect was also noted for concrete [16]. Ramulu *et al.* [17] machined metal-matrix-composites by HAE at shallow impact angles and observed erosion by microcutting in the matrix, whereas the inclusions were removed by the shovelling action of the water flow. Hamatani and Ramulu [18] used HAE to pierce compound ceramics. They found random damage generated by the hydro-abrasive jet on top of the pierced holes as well as non-linear hole tapers. They also detected a notable increase in the target temperature and concluded that HAE-machining of ceramics may be not totally free of thermal effects. Local micro-melting was observed by Savrun and Taya [19] in the matrix of SiC-reinforced aluminium.

Kahlman *et al.* [20] who proposed the formation of high local temperatures at the surfaces of ceramics during HAE introduced the idea of thermal spalling. They assumed that the sudden cooling of the heated sections by the water flow creates local stress fields. Based on SEM-photographs and wear volume measurements, the thermal shock resistance, R^*, was identified as the major resistance parameter against HAE, and a machining limit was defined for ceramics at $R^* = 15$ W/mm. Above this value, the material removal decreased rapidly. Exceptions were whisker-reinforced composites which was explained in [20] by heat dissipation through the whiskers. The results are summarized in Fig. 3. In a subsequent paper, these authors suggested

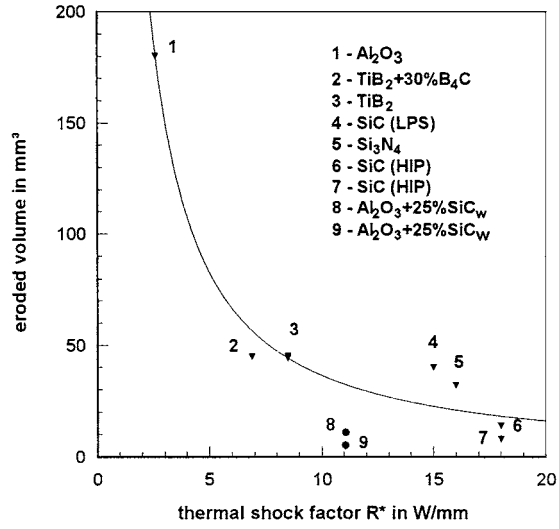

Figure 3 Relationship between thermal shock resistance and eroded volume in ceramics [20].

to use HAE as a testing method for sliding wear that involves high flash temperatures [21].

However, refractory ceramics of the type discussed in this paper are tension-softening materials [22, 23] which are able to transmit load perpendicular to the crack surface after crack initiation. This property can be characterized by a relationship between crack width (crack opening displacement, deformation; w) and stress (σ). This relationship is shown in Fig. 4 for two typical refractory ceramics. The area enveloped by the curves in Fig. 4 is the fracture energy [24]:

$$G_F = \int_0^{w_1} \sigma(w)\,\mathrm{d}w. \tag{1}$$

The influence of this fracture parameter on wear processes was probably first noted in [25]: it was found that the fracture energy can be related to the abrasion resistance of cementitious composites. More recently, it was shown that fracture energy can be used to describe other impact processes, such as comminution in mechanical crushers [26]. An approximation of $\sigma(w)$

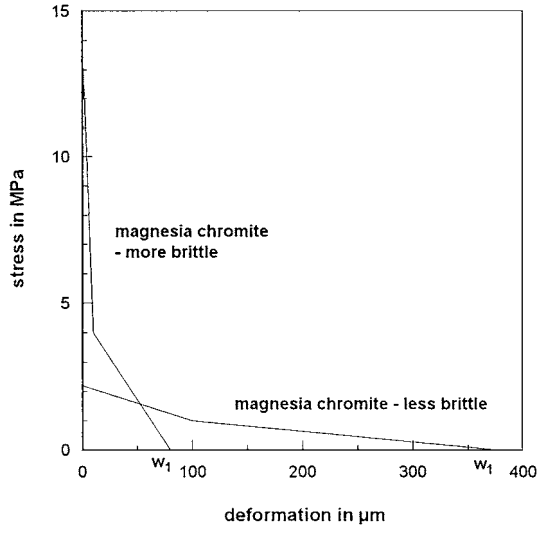

Figure 4 Stress-deformation-functions $\sigma(w)$ for two refractory ceramics [22].

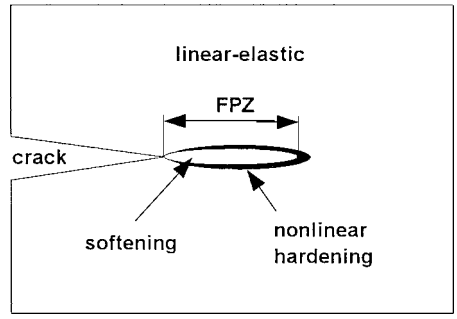

Figure 5 Fracture process zone in a quasi-brittle material.

for refractory ceramics is given in [23] as follows:

$$\sigma(w) = \frac{1}{(1 + w_1)^2}. \tag{2}$$

It was observed in [23] that the fracture process is characterized by the opening of pre-fabricated cracks, combined with crack-rim friction and grain bridging. These energy-dissipative mechanisms occur in a so-called fracture process zone (referred to as FPZ) as illustrated in Fig. 5. This parameter can be related to a characteristic length which is given as follows [24]:

$$L_{CH} = \frac{G_F \cdot E_M}{\sigma_t^2}. \tag{3}$$

In the equation, G_F is the fracture energy, E_M is Young's modulus, and σ_t is the tensile strength. These parameters, including the characteristic length, are listed in Table I for the materials investigated in this study. It was found that the characteristic length can efficiently be used to characterise the fluid erosion resistance [27, 28] and the impact resistance [29] of tension-softening materials. Two of the mechanisms responsible for the formation of a process zone are crack bridging and crack deflection, and these mechanisms could be observed during particle impact of alumina ceramics [30].

At that point, it is interesting to note that the thermal shock resistance applied in [20] to discuss the HAE of ceramics is closely related to the characteristic length, L_{CH}, of refractory materials [22]:

$$L_{CH} = 2 \cdot R^*. \tag{4}$$

TABLE I Mechanical properties of the investigated materials

Property	Material		
	Bauxite	Sintered magnesia	Magnesia chromite
Compressive strength (MPa)[a]	126	40	30
Bending strength (MPa)[a]	19	14	3.5
Young's modulus (GPa)	59	85	13
Density (g/cm³)	2.89	3.00	3.26
Porosity (%)	15	15 ± 2	15 ± 2
Crack extension force (J/m²)[b]	–	200	400
Fracture energy (J/m²)[b]	–	550	990
Characteristic length (mm)[b]	–	100	100

[a]Cold values.
[b]Internal measurements RHI Refractories GmbH, Mülheim.

This relationship offers an opportunity to discuss the erosion results reported in [20] from the point of view of non-linear fracture mechanics.

2. Properties and structure of the investigated materials

Three different types of commercial refractory ceramics, namely sintered magnesia, magnesia chromite, and bauxite, were used in this study. The mechanical properties of the materials are listed in Table I. Prior to the erosion experiments, the structure of several samples has been examined by X-ray spectroscopy and scanning electron microscope imaging.

Sintered magnesia bricks are used as lining material for steel and cement furnaces. It consists mainly of periclase (95%). It has a high melting point and a high Young's modulus, and behaves very brittle under mechanical load as illustrated in Fig. 6a. The chemical composition is given in Table II. The structure of the sintered magnesia used in the study is basically formed by a periclase matrix where periclase grains are embedded as shown in Fig. 6b. The inclusions consist of directly bonded crystals with diameters up to 160 μm. Between the crystals, gussets are formed. This is also shown in Fig. 6b. Due to etching, the gusset material was identified to be silica. The inclusion grains show a low porosity. However, the direct bond generates comparatively high bonding forces between the periclase crystals. Vickers indentations in periclase crystals showed slight deformations at the edge and short cracks originating from the indentation. The Vickers hardness

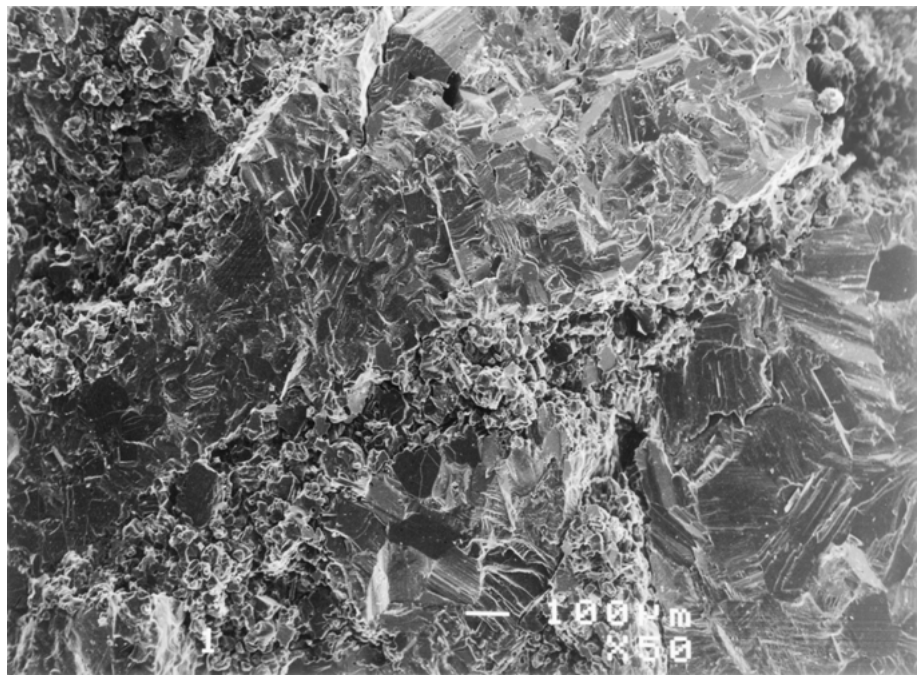

(a)

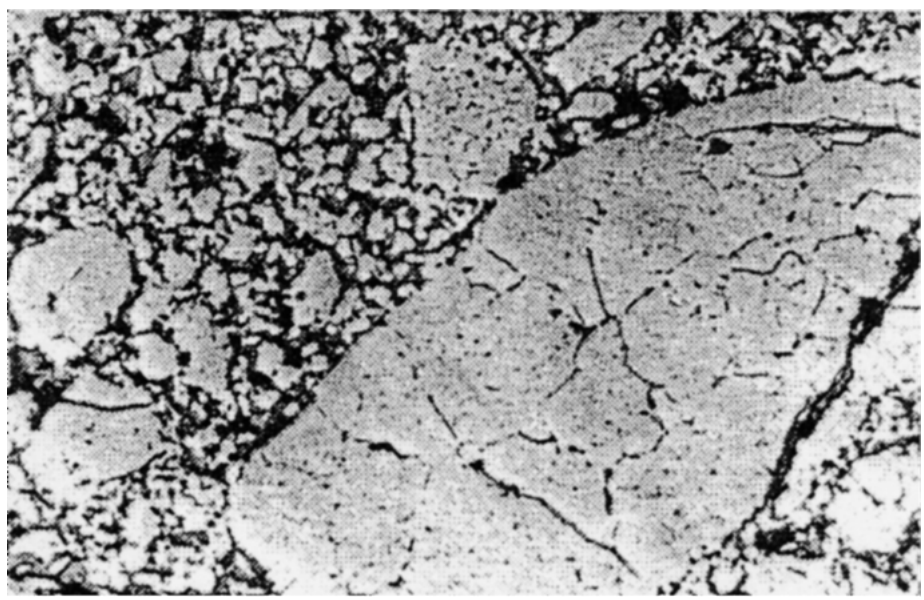

(b)

Figure 6 Structure and behaviour of sintered magnesia: (a) Brittle fracture under mechanical load and (b) Basic structure.

TABLE II Chemical compositions of the investigated materials

Element	Percentage (%)		
	Bauxite	Sintered magnesia	Magnesia chromite
Al_2O_3	81	0.1	6
Fe_2O_3	1.7	0.2	14
SiO_2	12	0.5	0.5
CaO	<0.4	2.1	1.3
MgO	<0.4	97	60
TiO_2	3.2	–	–
Cr_2O_3	–	–	18
$K_2O + Na_2O$	0.6	–	–

of matrix and inclusions was measured and delivered values of about $HV_{100} = 120$ kg/mm^2 for the matrix, and $HV_{100} = 700$ kg/mm^2 for the inclusions.

Magnesia chromite is used for the lining of steel and cement furnaces, and for non-ferrous metal kilns where high spalling resistance and high temperature resistance are needed. The chromite phase reduces the Young's modulus and induces some capability to plastic deformation. The chemical composition is given in Table II. The magnesia chromite used in the study consists of directly bonded chromite grains and periclase crystals as shown in Fig. 7. The white-appearing chromite particles are surrounded by the periclase crystals. Very often, the periclase is infiltrated by iron and chrome causing secondary spinell exsolutions (Fe, Cr, Al). This is probably one reason for the high values for the fracture energy G_F. Moreover, the periclase crystals are sometimes broken, probably due to the intense heat treatment during the manufacturing process. The chromite grains are comparatively dense with only a few closed pores. The chromite Vickers hardness ($HV_{100} = 1500$ kg/mm^2) is comparatively high compared to that of periclase ($HV_{100} = 500$ kg/mm^2). Vickers indentations in the chromite crystals showed pronounced cracking (see Fig. 7); indentations in the periclase did not show any cracking, but plastically deformed regions. The material consumes a rather large amount of energy during crack extension.

Bauxite bricks are commonly used in the steel industry. The material has a medium Young's modulus and a relatively high compressive strength. Generally, the temperature resistance is low. The chemical composition is given in Table II. From the point of view of phase composition, the material mainly contains corundum (50%–70%) and mullite (25%–35%). The chemical analysis identified the principal mineral phases as α-corundum, mullite, tialite, and titanium oxide. The SEM-image in Fig. 8 shows two large corundum grains (5 mm in length) that are sharply separated from the matrix by interfaces. The matrix consists of corundum, mullite and tialite. A close look at the matrix of the lower grain in Fig. 8 shows corundum grains (dark grey), and mullite (white grey). The very white reflecting areas are occupied by titanium oxide. The large corundum grains acting as inclusions consist of individual crystals, bonded by tialite and titanium oxide. The structure is porous.

3. Experimental set-up

The erosion facility used in this study to simulate HAE consisted of an intensifier pump to produce the high water pressure, a head for mixing and accelerating the abrasive particles, an abrasive storage and metering system, a catcher, and an x-y-z-positioning table. The head, which hosts a chamber for the mixing between the high-speed water jet and the entrained abrasive particles as well as a focus for accelerating the abrasive particles, is shown in Fig. 9. The erosion conditions as well as the parameters varied during the erosion tests are listed in Table III. The variable parameters included abrasive particle velocity, local exposure time, abrasive mass-flow rate, and abrasive type.

Depth and width of any eroded cavity were estimated as the average of five measurements. The specific

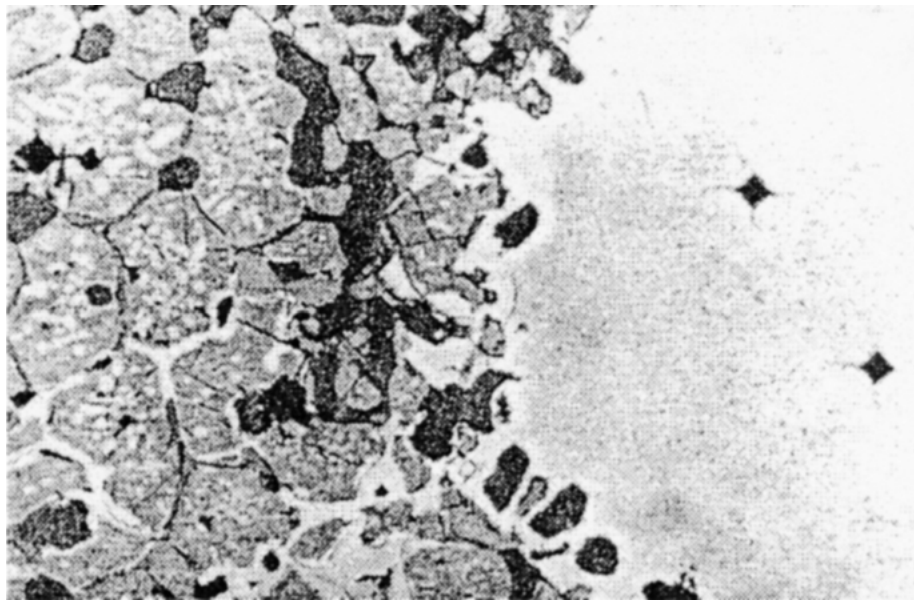

Figure 7 SEM-image of the magnesia chromite structure.

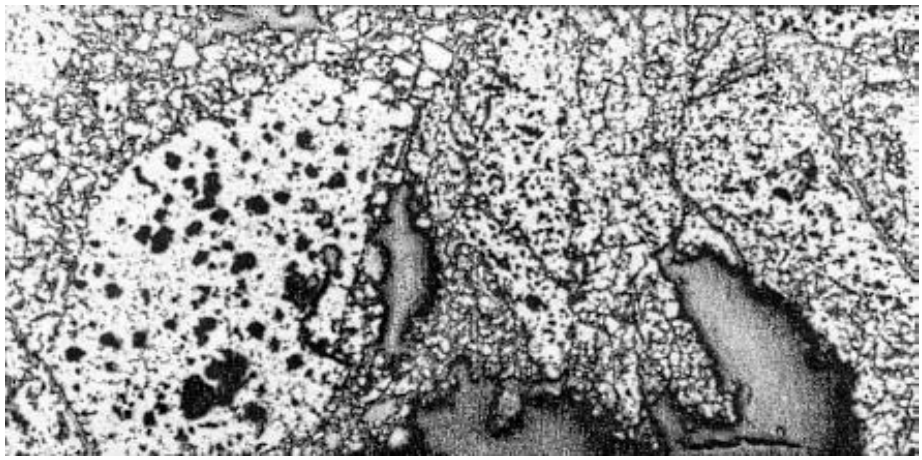

Figure 8 SEM-image of the bauxite structure.

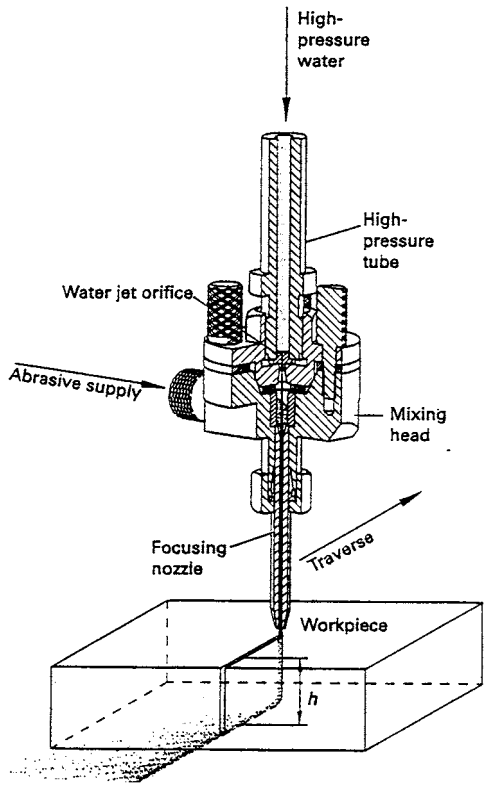

Figure 9 Experimental set-up.

erosion rate, E_R, rate was calculated as follows:

$$E_R = \frac{h \cdot b \cdot v_T}{\dot{m}_P}, \tag{5}$$

where h is the erosion depth, b is the eroded width, v_T is the traverse rate of the machining head, and $\dot{m}_P$ is the abrasive mass-flow rate. Because the erosion rate is the ratio between the volumetric removal rate and the abrasive mass-flow rate, it is given in mm^3/g.

To understand the material removal processes involved in the HAE of the ceramics, optical microscope and scanning electron microscope (referred to as SEM in the paper) were used to inspect the erosion sites. Typically, the HAE entry zone (top of the cut) and the HAE exit zone (bottom of the cut) are examined.

TABLE III Erosion conditions

Fixed parameters	
Abrasive particle shape	Angular
Orifice material	Sapphire
Orifice diameter (mm)	0.39
Focus length (mm)	89.0
Focus diameter (mm)	1.27
Stand-off distance (mm)	6.0
Impact angle (°)	90
Method of abrasive feed	Suction
Abrasive condition	Dry
Variable parameters	
Abrasive type	Garnet #36
	Corundum #100
Abrasive hardness (HV)	
Corundum	2250
Garnet	1500
Abrasive mass-flow rate (g/s)	4.5; 6.1; 7.4; 10.6; 14.3; 19.1
Abrasive particle velocity (m/s)	260; 310; 380; 440; 475; 515
Local exposure time (sec)	0.10; 0.16; 0.21; 0.32; 0.64; (1.27)

4. Experimental results and discussion

4.1. Influence of the abrasive particle velocity

Fig. 10 shows the influence of the abrasive particle velocity for different target materials as well as for different abrasive types on the erosion rate. The abrasive particle velocity was approximated by the following relationship [1]:

$$v_P = \frac{\alpha \cdot \phi \cdot \sqrt{p}}{\sqrt{\rho_W} \cdot (1 + \dot{m}_P/\dot{m}_W)}, \tag{6}$$

where α and ϕ were estimated by jet impact-force measurements [1, 31]. In the equation, p is the pump pressure, ρ_W the fluid density, $\dot{m}_P$ the abrasive mass-flow rate, and $\dot{m}_W$ the fluid mass-flow rate. The general trend as shown in Fig. 10 was observed under all erosion conditions and for all materials. It agrees with results in [28]. The mathematical expression is a power law of the type

$$E_R = C_1 \cdot (v_P - v_{PT})^n, \tag{7}$$

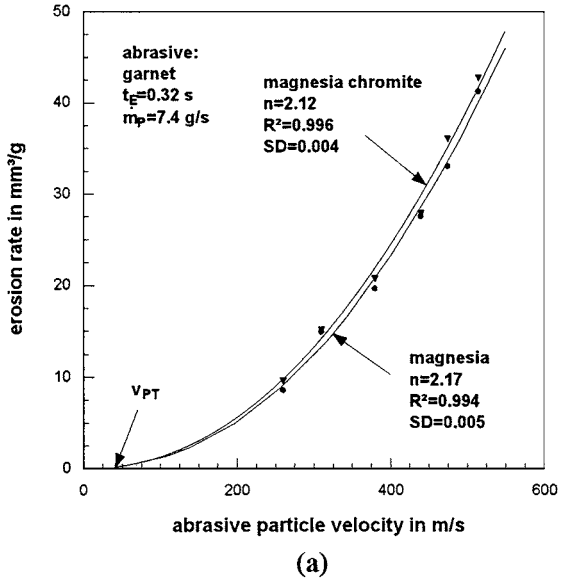

Figure 10 Relationship between abrasive particle velocity and erosion rate: (a) Target material influence and (b) Abrasive type and exposure time influence.

where the parameter v_{PT} is a critical abrasive velocity which must be exceeded to introduce the damage process under the given conditions, and n is a power exponent. There is some evidence from solid-particle erosion experiments on ceramics [32] as well as from HAE-experiments on concrete [33] that the threshold velocity may be related to the bar wave velocity, usually defined as:

$$v_W = \sqrt{E_M/\rho_M}. \tag{8}$$

However, despite the notable differences in Young's modulus and the comparative densities of sintered magnesia and magnesia chromite, the threshold values are quite similar for both materials ($v_{PT} = 40$ m/s) as shown in Fig. 10a. Interestingly, the characteristic lengths of these materials according to Equation 5 are of a comparative order, and it seems that this parameter balances the threshold conditions for failure. It could be that the capability to dissipate energy in the neighbourhood of the growing cracks plays an important role. Such mechanisms were recently identified during the hydro-erosive wear of cementitious composites [34]. However, more systematic studies are required to verify this assumption.

It is further interesting to note from Fig. 10b that the threshold velocity of the bauxite is not very sensitive to the abrasive type. The threshold velocity is $v_{PT} =$ 25 m/s for corundum (harder abrasive material) and about $v_{PT} = 30$ m/s for garnet (softer abrasive material). In contrast, the established erosion process ($v_P > v_{PT}$) is notably influenced by the abrasive type. If corundum is used instead of garnet, the erosion rate more than doubles at an abrasive particle velocity of $v_P = 475$ m/s. Therefore, the constant C_1 in Equation 7 is very sensitive to the abrasive type.

The power exponent n in Equation 6 was estimated by geometric regressions ($Y = AX^n$) of the results; the coefficient of regression was always larger than $R^2 =$ 0.99, and the standard deviation was always less than $SD = 0.005$ (all regression parameters are shown in Fig. 10a and b). For equal erosion conditions, the power exponent shows only a slight dependence of the material type: It is $n = 2.17$ for sintered magnesia and $n = 2.12$ for magnesia chromite. These values are close to power exponents estimated by Ritter [35] for dry solid particle erosion ($n = 2$). Assuming inclusion pull-out as the dominating material removal mode, this author found a distinct relationship between the impacting particles' kinetic energy and the material removal in structural ceramics. However, for a comparative long local exposure time ($t_E = 1.27$ s) as shown in Fig. 10b the power exponent drops to $n = 1.61$ (for corundum) which has never been reported for solid particle erosion of ceramics. It could, however, be assumed that liquid film damping due to water trapped in the eroded cavity may partly be responsible for this reduction in the erosion progress. These damping effects are very likely because the application of a long exposure time and the rather hard abrasive material allows the formation of comparatively deep and narrow erosion kerfs in the resistant target material. Similar observations are reported in [16] where it was noted that damping is more severe in erosion resistant materials. However, more information is needed to suitably discuss this interesting phenomenon. It was also noted that n increases as the abrasive hardness decreases (see Fig. 10b) and particle size increases.

Certain interesting conclusions can be drawn from these observations: Firstly, in the threshold range ($v_P < v_{PT}$) neither conventional material properties nor abrasive particle type significantly influence the basic material removal process. However, it seems that non-linear fracture parameters play a role. The influence of the abrasive type increases as abrasive particle velocity increases (which means higher effective stress). In an investigation of the erosion of ceramics by abrasive water jets, Wada [10] defined wear maps showing the erosion mode as a function of the effective stress, σ_E, and the hardness-ratio target/abrasive, $R_H = H_M/H_P$ (see Fig. 2). In a wear map for a given material, the material removal mode shifts from scratching for moderate

effective stress and moderate H_M-value to lateral cracking for a high effective stress and a low H_M-value. It is known that the hardness of an abrasive particle plays a dominating role if particles impinge at a low angle. For higher impact angles, especially at orthogonal impact, the fracture toughness of the target material predominates the erosion process. These effects were noted by Hashish [36] for the HAE of ceramic focusing nozzles, and by Bell and Rogers [37] as well as by Wang *et al.* [38] for the solid particle erosion of ceramics. Therefore, at the introduction stage of HAE ($v_P < v_{PT}$) where the target is hit at almost orthogonal angles, differences in hardness are not significant. If the HAE-process is fully introduced ($v_P \gg v_{PT}$) and a pit is generated, the particles start to impinge the target surface at shallower angles and hardness controls the erosion process. This situation is simplified by the illustrations in Fig. 10b. If the pit grows further, damping effects due to a water film or due to a water-grit-suspension at the bottom of the pit influence the erosion process; especially if the target material has a high HAE-resistance.

4.2. Influence of the local exposure time

The local exposure time is given by:

$$t_E = \frac{d_F}{v_T}. \tag{9}$$

In the equation, d_F is the focus nozzle diameter, and v_T is the traverse rate of the machining head. The influence of the local exposure time on the erosion rate is shown in Fig. 11a. The figure also contains some results obtained on concrete specimens eroded under equal conditions. For the given parameter range the relationships can reasonably be approximated by a hyperbolic equation:

$$E_R = \frac{C_2}{t_E}. \tag{10}$$

However, assuming $E_R = 0$ for $t_E = 0$, a maximum must appear in the function. Therefore, an optimum exposure time exists which should be smaller than $t_E = 0.16$ s for the materials tested in this study.

The erosion process is very sensitive against modifications in the local exposure time in a critical range between 0.1 s and 1 s. Beyond this limit (t_{EC}), there is no significant change in the erosion rate with an increase in the local exposure time, although there is a very slight decrease. These observations are important for milling and turning of refractory materials by HAE since they suggest that the material removal is more efficient at a short exposure time (which corresponds to a high traverse rate of the machining head). The application of several, very short machining steps is, therefore, more efficient than a single, rather long machining step. This applies especially to materials with a lower HAE-resistance. On the other hand, the use of a long exposure time guarantees a stable machining process since fluctuations in the machine's traverse regime do not notably influence the erosion rate. The value for t_{EC} obviously depends on the material type. For more resistant materials with high strength values, such as the bauxite, it is rather low. This is illustrated in Fig. 11b showing the relationship between critical local exposure time and compressive strength.

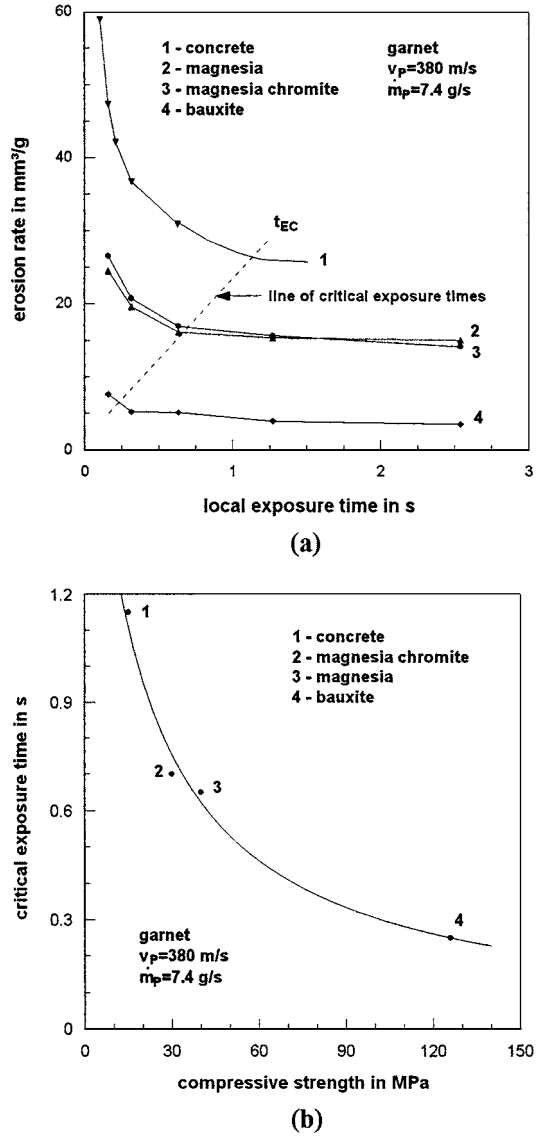

Figure 11 Relationship between local exposure time and erosion rate: (a) Target material influence and (b) Compressive strength and critical local exposure time.

Two preliminary conclusions can be drawn: Firstly, the higher compressive strength or the lower density, respectively, the lower the critical exposure time. Secondly, the higher compressive strength or the lower density, respectively, the less sensitive the material responses to a short local exposure time.

4.3. Influence of the abrasive mass-flow rate

Fig. 12 shows the relationship between abrasive mass-flow rate and erosion rate. The general trend is a relationship very similar to Equation 10.

$$E_R = \frac{C_3}{\dot{m}_P}. \tag{11}$$

The use of high abrasive mass flow rates deteriorates the erosion rate. The influence of the abrasive mass flow

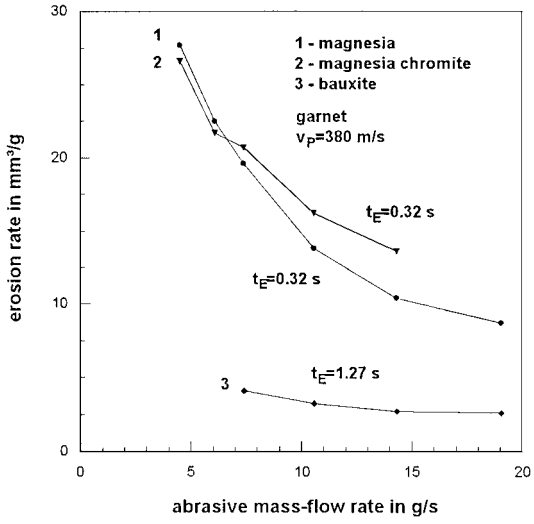

Figure 12 Relationship between abrasive mass flow rate and erosion rate.

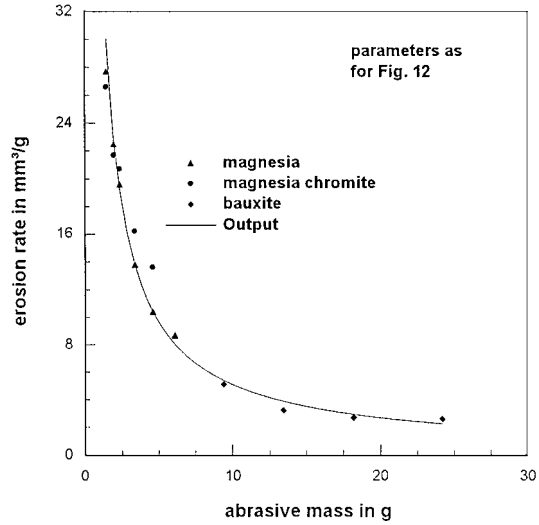

Figure 13 Relationship between absolute abrasive mass and erosion rate (parameters as for Fig. 12).

rate seems to drop if high-resistant materials (bauxite) and long exposure times are applied. Because the erosion rate must be zero for $\dot{m}_P = 0$, a maximum in the functions must appear at abrasive mass flow rates lower than $\dot{m}_P = 4.5$ g/s. It is very interesting to note that sintered magnesia and magnesia chromite behave equally in the range of low abrasive mass-flow rates. The absolute values of the erosion rate as well as the progress of the functions are almost equal. However, beyond a level of about $\dot{m}_P = 7$ g/s the functions for the materials are very different. In this range, the sintered magnesia shows a significant decrease in the erosion rate with rising abrasive mass-flow rate, whereas the erosion rate in the magnesia chromite does not notably drop. The function for the bauxite was estimated with a different local exposure time. Therefore, a quantitative comparison is not possible. However, the general trend agrees with those of the other two materials. The curve obtained for the bauxite again illustrates the observation from Section 3.2 that a comparatively high local exposure time guarantees a stable erosion process even if the abrasive mass flow rate remarkably changes.

In order to directly compare the three materials, a new parameter, the abrasive mass

$$M_P = \dot{m}_P \cdot t_E, \tag{12}$$

is introduced. This is the absolute abrasive mass involved in the erosion during the local exposure time. The results of this modification are shown in Fig. 13. Note that the experimental points of any material are located on a single line which can be approximated by:

$$E_R = \frac{C_4}{M_P^k} = \frac{C_4}{(\dot{m}_P \cdot t_E)^k}. \tag{13}$$

For the materials and the test conditions in this study, $C_4 = 42.18$, and $k = 0.92$. However, from Equations 11 and 12, k should be unity. The small deviation is due to the approximations made to derive Equation 13.

As the functions for exposure time and abrasive mass-flow rate are very similar in their general trend, the behaviour of the materials could be discussed in terms of the absolute number of impacting abrasive particles. If local exposure time and abrasive mass-flow rate increase, the number of impacting particles increases. This relationship is actually expressed by Equation 12.

Because the average abrasive impact velocity (impact energy, respectively) decreases with an increase in the abrasive mass-flow rate due to mixing losses [1], an increase in the abrasive mass-flow rate does not improve the material removal process in the materials. However, the magnesia chromite has shown some capability to plastically deform during the Vickers indentation tests. Therefore, it may absorb a certain amount of the energy prior to fracture. Moreover, this material absorbs a comparatively high amount of energy during crack extension (see the high values for G_{Ic} and G_F; Table I). Thus, multiple particle impact supports the erosion process in this material. As the frequency (particle number per time period) of impacting particles increases, the material removal process may partly improve. Therefore, the drop in erosion rate is rather low for this material. In contrast, the very brittle-behaving sintered magnesia (see Fig. 6a) is more sensitive to the impact energy of the individual particles than to the particle impact frequency. An increase in impact frequency has no notable effect. Therefore the drop in erosion rate is more severe in this material compared to the magnesia chromite. These phenomena may cause the different trends for magnesia and magnesia chromite for high abrasive mass flow rates shown in Fig. 12. These observations also show that the equal behaviour for both these materials as presented in Fig. 10a is valid for comparatively low abrasive mass-flow rates only.

5. Material removal process observations

5.1. Sintered magnesia

Fig. 14a shows an SEM-photograph of the upper erosion zone of a magnesia sample. Matrix and inclusion

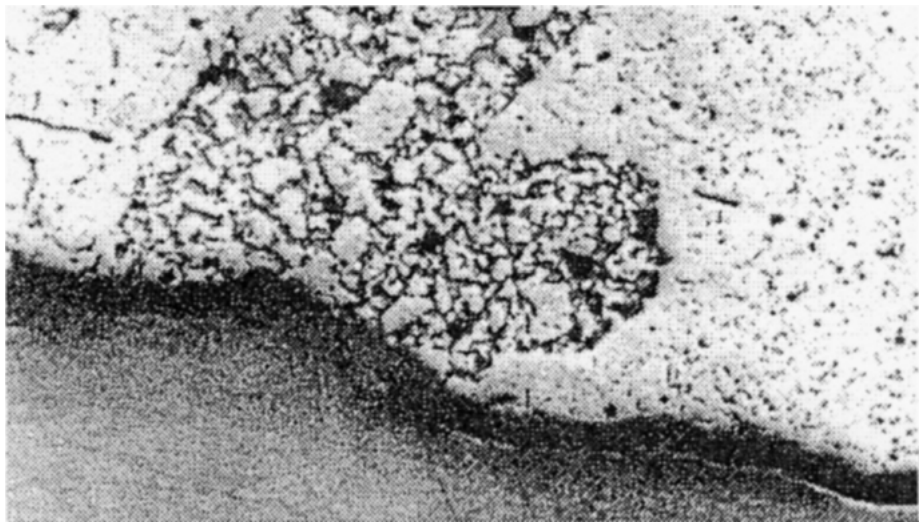

(a)

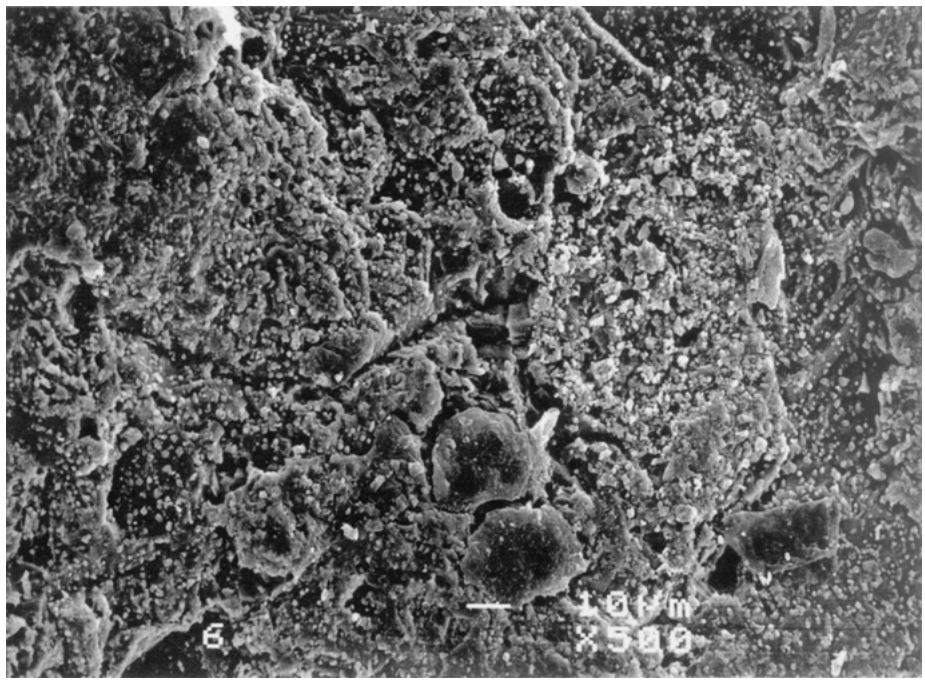

(b)

Figure 14 SEM-images of eroded sintered magnesia: (a) Upper kerf region and (b) Lower kerf region.

are equally eroded. The interface between the periclase grains and the surrounding matrix is intact. At a higher magnification, open pores with sharp edges could be noticed as observed during the brittle fracture of the material in the tensile test (see Fig. 6a) as well as periclase fragments. Obviously, the periclase grains are fractured due to HAE. The material removal process can be characterised by a steady transgranular fracture through matrix and inclusions.

The situation is quite different in Fig. 14b taken from the lower zone of the same erosion site. Here, the periclase grains are completely intact (left region) or partially cracked (central region), but the matrix between them is removed. The figure shows that penetrating cracks are stopped by the hard periclase inclusions. In the light of Equation 1, this interesting feature of non-linear fracture deserves further investigation. No open pores were found. These observations indicate an intergranular material removal mode in the lower region. The small particles attached to the periclase surface are brucite particles formed due to the hydration of the magnesia oxide in the periclase grains after the erosion experiments.

5.2. Magnesia chromite

Some failure mechanisms observed in the chromite magnesia are shown in Fig. 15. In Fig. 15a, matrix removal can be noted. Most interestingly, the surrounded periclase inclusion is broken but not removed. The crack running through the grain can clearly be seen. Higher magnification showed slight branching of the crack. Again, this feature of non-linear fracture might be of special interest. As illustrated in Fig. 15b, the fracture surfaces generated in the periclase are comparatively large and regular. In a lower region of the kerf, large and undamaged periclase grains as well as groups of unbroken chromite grains could be noted.

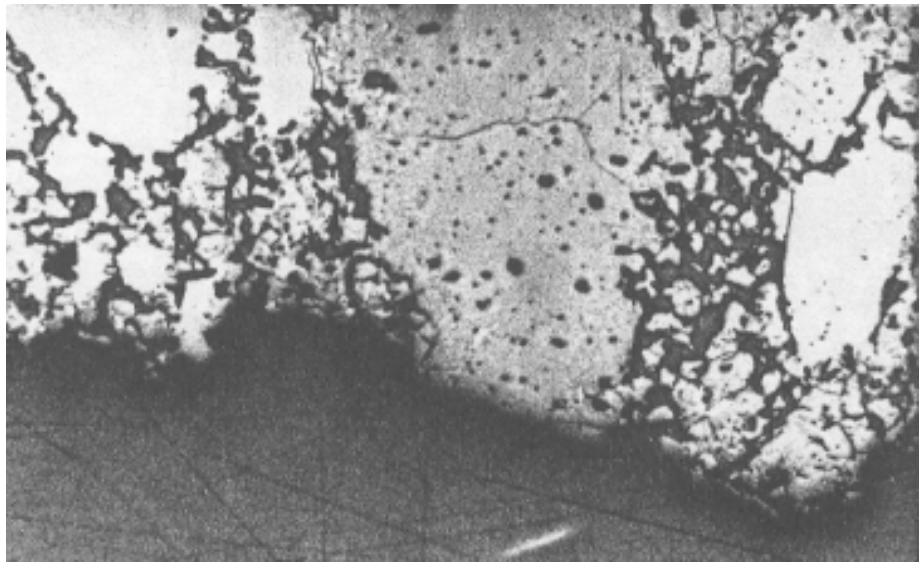

(a)

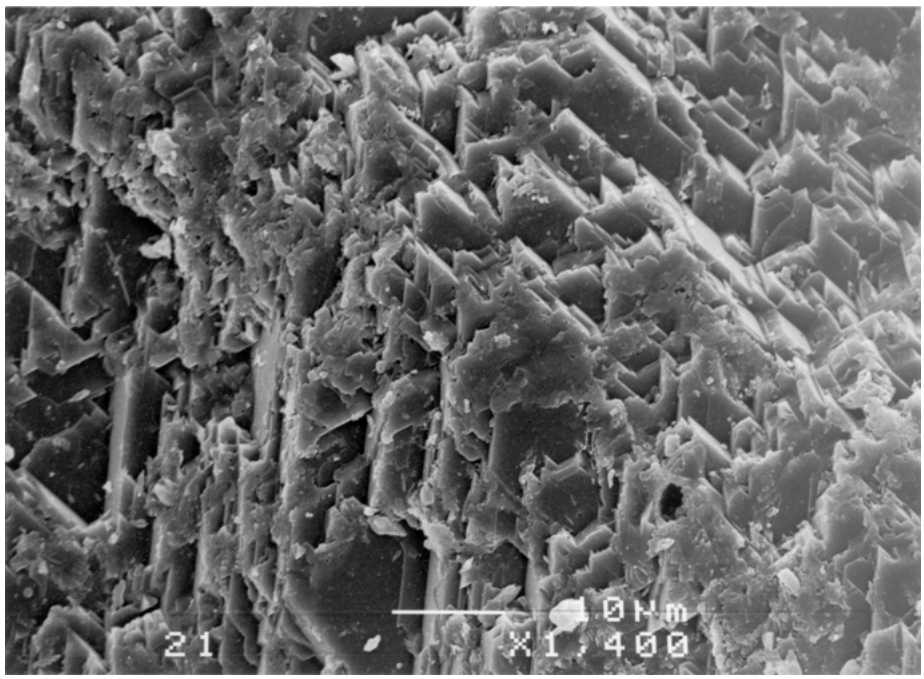

(b)

Figure 15 Images of eroded magnesia chromite: (a) General features and matrix erosion (optical microscope, 35×) and (b) Brittle erosion on a periclase inclusion (SEM).

5.3. Bauxite

Material removal features of HAE of bauxite are in detail investigated in [14] due to acoustic emission technique. It was found that the certain erosion mode depends on the energy delivered to the erosion site. Fig. 16a, which is an SEM-photograph from the lower region of a kerf, shows the surface of a corundum grain. Note that no pores are opened due to HAE; thus just the interface between inclusion and surrounding matrix is removed. The grain structure remained intact after HAE. The situation is different in Fig. 16b showing a destroyed corundum grain; individual corundum crystals are broken or completely exposed. There is some evidence of a continuous crystal-by-crystal fracture. This figure was taken from an erosion site generated by abrasives with high velocities.

5.4. General observations

A systematic observation of the entire erosion front (from the entry to the exit) did not give any indication of an abrupt change in the material removal mode for the investigated materials. The transition from transgranular fracture at the top region to an intergranular removal at the bottom region of the kerf was steady. This result supports the idea of a continuous energy loss of the abrasive particles in the kerf as supposed by Momber and Kovacevic [39, 40] and Raju and Ramulu [41]. At the first stage of HAE, the individual abrasive grains have sufficient kinetic energy to introduce the erosion in any individual part of the material. In the upper region, their energy is high enough to cut the harder inclusions (periclase Vickers hardness for example was measured to be about 700 kg/mm^2). However, due to friction, damping

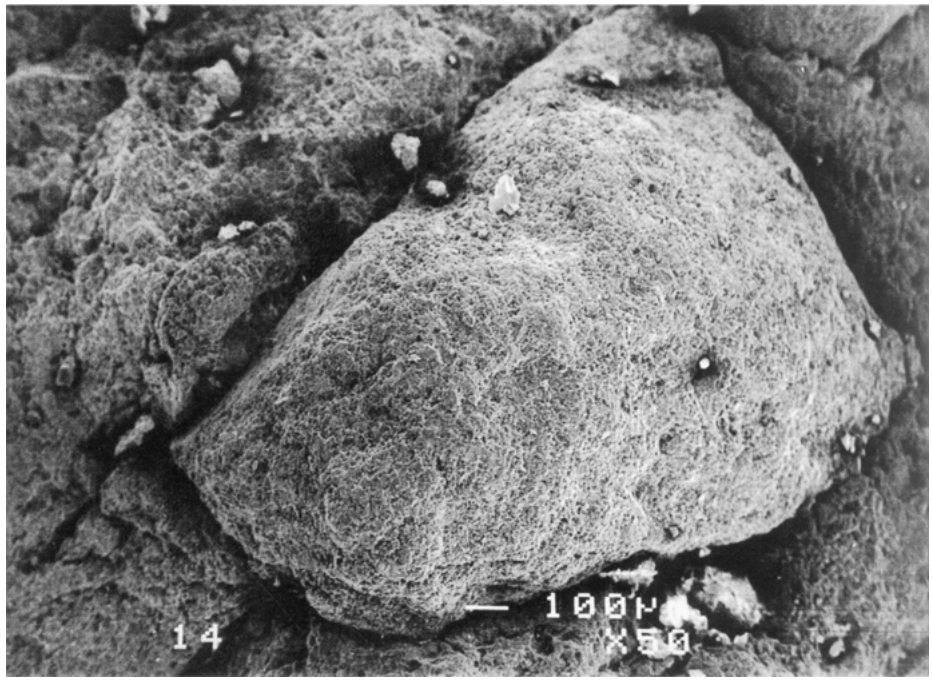

(a)

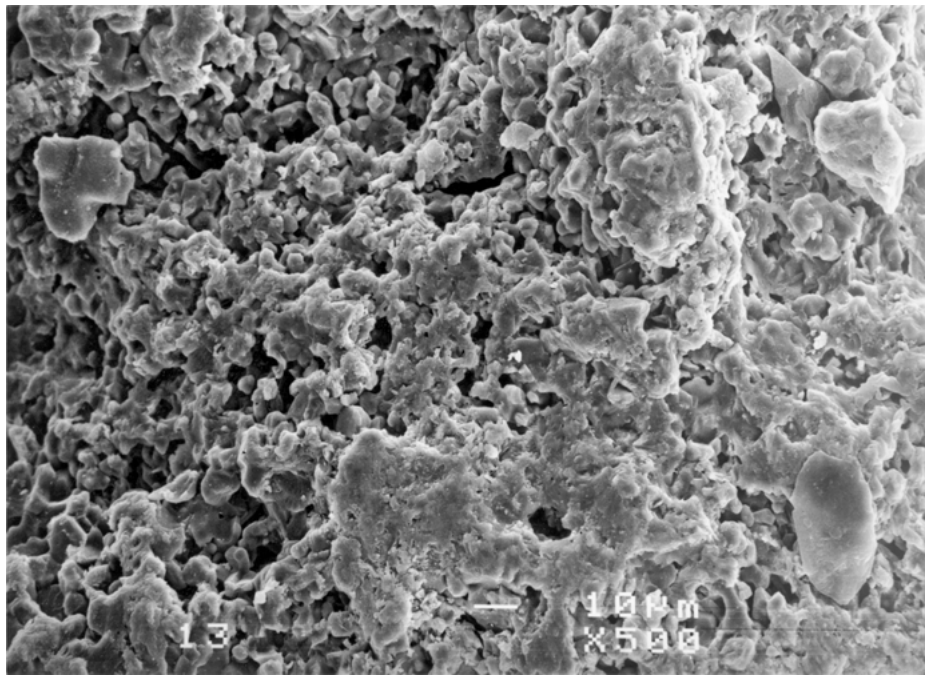

(b)

Figure 16 SEM-images of eroded bauxite: (a) Intergranular erosion of a corundum inclusion and (b) Erosive fracturing of corundum crystals.

and generation of wear debris, the abrasives lose part of their kinetic energy. In the lower region of the kerf, the particles having a reduced kinetic energy can no longer destroy the inclusions, but can only remove the weaker matrix between individual inclusions.

For a moderate abrasive velocity, this unsteady erosion mode is reflected by the structure of time-domain acoustic emission signals (denoted AE) acquired during HAE. As shown in Fig. 17, the AE-signals of a bauxite specimen show several burst emissions. This type of emission usually corresponds to events of sudden energy release, such as spall fracture. Probably, these burst emissions express the fracture of inclusion grains [14, 16]. This process generates high-energy stress waves which are detected by the AE-technique. In contrast, the continuous base signal may result from the matrix erosion.

Some restricted features of non-linear fracture (crack arrest, crack branching) have been noted. These preliminary observations open up a way to discuss the HAE of refractory ceramics alternatively. In particular, non-linear fracture parameters, such as fracture energy and characteristic length (see Equations 1 and 3), could be estimated and related to typical erosion parameters. Earlier HAE-results obtained on ceramics [7, 20] and rocks [8] can be reconsidered by introducing non-linear fracture mechanics. One example is shown in Fig. 18 where the results from [20] (shown in Fig. 3)

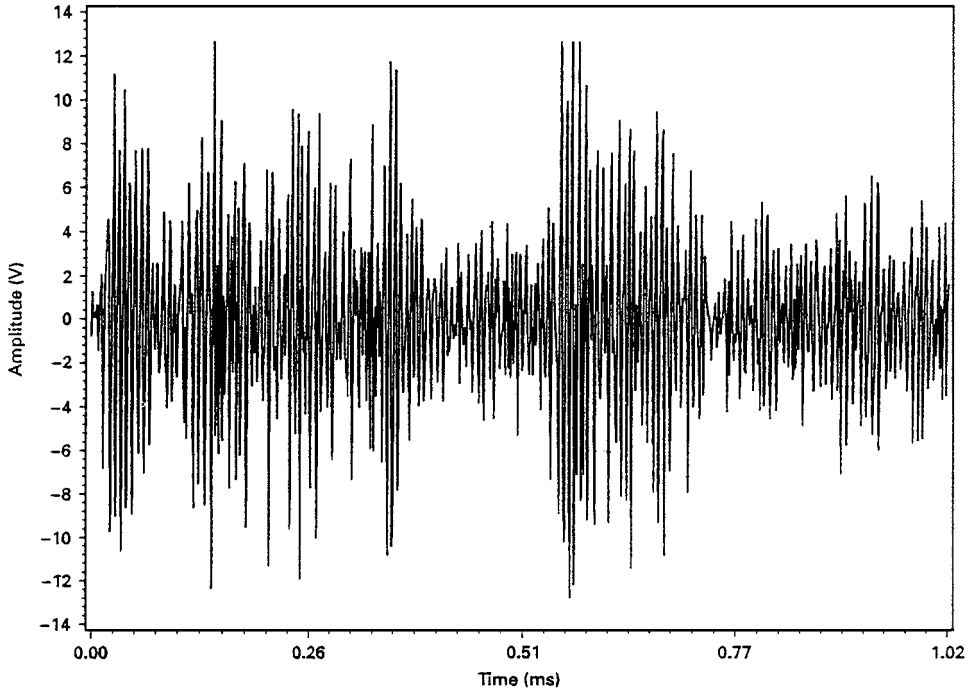

Figure 17 Time-domain AE-signal acquired from an eroded bauxite specimen [2]; $v_P = 380$ m/s, $\dot{m}_P = 7.4$ g/s, $t_E = 1.27$ s.

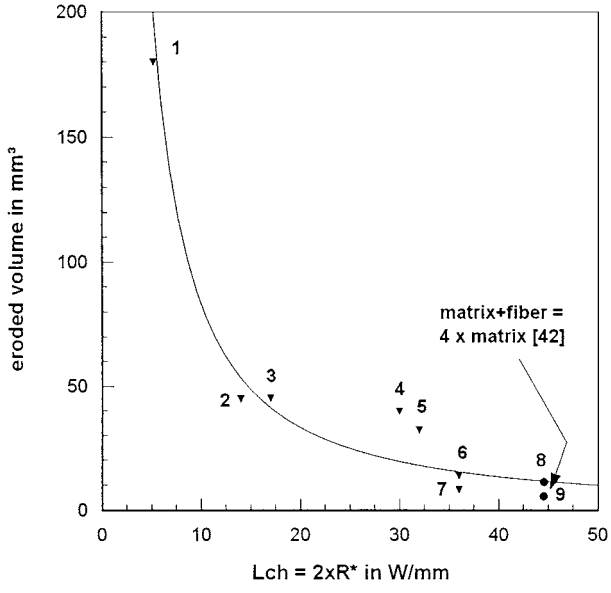

Figure 18 Relationship between characteristic length and eroded volume in ceramics (same results as used for Fig. 3).

are redrawn. Note the improvement in the trend for the whisker-reinforced ceramics if L_{CH} is used instead of R^* (see Equation 4).

6. Summary

The results of this study can be summarised as follows:

– HAE can generally be utilised to machine high-quality refractory ceramics (bauxite, sintered magnesia, magnesia chromite).

– Erosion rates between $E_R = 2.5$ mm^3/g and 300 mm^3/g can be achieved. A high abrasive velocity, low local exposure time, and medium abrasive mass-flow rate are beneficial to HAE. The use of corundum as abrasive material doubles the efficiency compared to garnet for the materials investigated in this study.

– The optimum process parameter constellation, especially the evaluation of the abrasive mass-flow rate, is strongly related to the behaviour of the eroded material.

– The material removal process is a mixture between transgranular fracture and intergranular failure. The balance between both modes depends on the energy delivered to the erosion site. These observations are explained by assuming a continuous loss in kinetic energy of the abrasive particles during HAE.

– It is suggested to consider non-linear fracture parameters to discuss HAE of refractory ceramics.

Acknowledgements

The authors are thankful to Mr. I. Eusch for his help during the experiments. The use of facilities at the Institut für Gesteinshüttenkunde, Montan Universität Leoben, Austria, where scanning electron microscopy and X-ray spectroscopy were completed is appreciated. The authors are also thankful to Veitsch Radex AG, Austria, for providing the refractory specimens.

References

1. A. W. MOMBER and R. KOVACEVIC, "Principles of Abrasive Water Jet Machining" (Springer Verlag Ltd., London, 1998).
2. A. W. MOMBER, I. EUSCH and R. KOVACEVIC, *J. Mater. Sci.* **31** (1996) 6485.
3. A. LAURINAT, "VDI-Fortschritt-Berichte, Reihe 2: Nr. 327" (Düsseldorf, VDI-Verlag, 1994).
4. R. KOVACEVIC, H. S. KWAK and R. S. MOHAN, *Inst. Mech. Engrs. J. Eng. Manuf.* **212** (1998) 45.
5. T. J. KIM, G. SYLVIA and L. POSNER, *ASME PED* **17** (1985) 19.
6. B. FREIST, H. HAFERKAMP, A. LAURINAT and H. LOUIS, in "Proc. of the 5th American Water Jet Conference," edited by M. M. Vijay and G. A. Savanick (St. Louis, Water Jet Techn. Assoc., 1989) p. 191.

7. D. C. HUNT, T. J. KIM and J. G. SYLVIA, in "Proc. 8th Int. Symp. Jet Cutting Techn." (Cranfield: BHRA, 1986) p. 287.
8. S. MATSUI, H. MATSUMURA, Y. IKEMOTO, Y. KOMUN and H. SHIMIZU, in "Proc. 6th Amer. Water Jet Conf." (St. Louis, WJTA, 1991) p. 31.
9. S. WADA and Y. KUMON, *J. Ceram. Soc. Japan, Int. Edit*. **101** (1993) 830.
10. S. WADA, *ibid*. **104** (1996) 247.
11. I. M. HUTCHINGS, *J. Phys. D: Appl. Phys*. **25** (1992) A212.
12. J. ZENG and T. J. KIM, *Wear* **193** (1996) 207.
13. *Idem.*, *ibid.* **199** (1996) 275.
14. A. W. MOMBER, R. S. MOHAN and R. KOVACEVIC, *ASM J. Mater. Eng. Perform.* **8** (1999) 450.
15. K. A. SCHWETZ, L. S. SIGL, J. GREIM and H. KNOCH, *Wear* **181–183** (1995) 148.
16. A. W. MOMBER, R. S. MOHAN and R. KOVACEVIC, *Theoret. and Appl. Fracture Mech.* **31** (1999) 1.
17. M. RAMULU, S. P. RAJU, H. INOUE and J. ZENG, *Wear* **166** (1993) 55.
18. G. HAMATANI and M. RAMULU, *ASME J. Eng. Mater. Technol.* **112** (1990) 381.
19. E. SAVRUN and M. TAYA, *J. Mater. Sci.* **23** (1988) 1453.
20. L. KAHLMAN, S. KARLSSON, R. CARLSSON and C. G. NILSSON, *Amer. Ceram. Soc. Bull.* **72** (1993) 93.
21. L. KAHLMANN, K. M. ÖJMERTZ and L. K. FALK, *Wear* **248** (2001) 16.
22. H. HARMUTH and E. TSCHEGG, *Fatigue Frac. Eng. Mater. Struc*. **30** (1997) 1585.
23. H. HARMUTH, *World Cement Res. and Develop*. Oct. (1995) 71.
24. A. HILLERBORG, M. MODEER and P. E. PETERSEN, *Cement & Concr. Res*. **6** (1976) 773.
25. X. H. ZHANG and Y. Y. HUANG, in "Fracture Toughness and Fracture Energy of Concrete," edited by F. H. Wittmann (Elsevier, Amsterdam, 1986) p. 561.
26. A. W. MOMBER, *Eng. Fract. Mech*. **70** (2003) 81.
27. *Idem.*, *Int. J. Fract.* **112** (2002) 99.
28. *Idem.*, *Wear* **250** (2001) 100.
29. *Idem.*, *Theoret. & Appl. Fract. Mech*. **38** (2002) 151.
30. R. M. ANDERSON, T. A. ADLER and J. A. HAWK, *Wear* **162–164** (1993) 1073.
31. A. W. MOMBER, *Exp. Heat and Fluid Sci.* **25** (2001) 31.
32. G. A. EVANS, M. E. GULDEN and M. ROSENBLATT, *Proc. Roy. Soc. London, Ser.* A **361** (1978) 343.
33. A. W. MOMBER and R. KOVACEVIC, *Int. J. Rock Mech. Min. Sci.* **34** (1997) 17.
34. A. W. MOMBER, *Composites—Part B: Engineering* **34** (2003) 135.
35. J. E. RITTER, *Mater. Sci. and Eng.* **71** (1985) 195.
36. M. HASHISH, *ASME J. Tribol.* **116** (1994) 439.
37. J. F. BELL and P. S. ROGERS, *Mater. Sci. Techn*. **3** (1987) 807.
38. D. F. WANG, J. H. SHE and Z. M. MA, *Wear* **180** (1995) 35.
39. A. W. MOMBER and R. KOVACEVIC, *Inst. Mech. Engrs., J. Manuf. Eng.* **209** (1995) 491.
40. *Idem.*, *Inst. Mech. Engrs., J. Tribol. Eng.* **213** (1999) 463.
41. S. P. RAJU and M. RAMULU, in "Manufacturing Science and Engineering," Vol. 1. (New York, ASME, 1994) p. 339.
42. C. T. YU and A. S. KOBAYASHI, *Ceram. Engng. and Sci. Proc.*, **14**(7/8) (1993) 273.

Received 29 August 2002
and accepted 27 February 2003